Morio Tomizawa[1]
Department of Mechanical Engineering,
The University of Tokyo,
71C2, 2nd Bldg-Eng.,
7-3-1 Hongo,
Bunkyo-ku, Tokyo 113-8656, Japan
e-mail: tomizawa@hnl.t.u-tokyo.ac.jp

Keisuke Nagato
Department of Mechanical Engineering,
The University of Tokyo,
71D4, 2nd Bldg-Eng.,
7-3-1 Hongo,
Bunkyo-ku, Tokyo 113-8656, Japan
e-mail: nagato@hnl.t.u-tokyo.ac.jp

Kohei Nagai
Department of Mechanical Engineering,
The University of Tokyo,
71C2, 2nd Bldg-Eng.,
7-3-1 Hongo,
Bunkyo-ku, Tokyo 113-8656, Japan
e-mail: nagai@hnl.t.u-tokyo.ac.jp

Akihisa Tanaka
Department of Mechanical Engineering,
The University of Tokyo,
71C2, 2nd Bldg-Eng.,
7-3-1 Hongo,
Bunkyo-ku, Tokyo 113-8656, Japan
e-mail: tanaka.a@hnl.t.u-tokyo.ac.jp

Marcel Heinzmann
Institute for Applied Materials − Electrochemical
Technologies (IAM-ET),
Karlsruhe Institute of Technology (KIT),
Adenauerring 20b,
Karlsruhe 76131, Germany
e-mail: marcel.heinzmann@kit.edu

André Weber
Institute for Applied Materials − Electrochemical
Technologies (IAM-ET),
Karlsruhe Institute of Technology (KIT),
Adenauerring 20b,
Karlsruhe 76131, Germany
e-mail: andre.weber@kit.edu

Gen Inoue
Department of Chemical Engineering,
Kyushu University,
744 Motooka,
Nishi-ku, Fukuoka 819-0395, Japan
e-mail: ginoue@chem-eng.kyushu-u.ac.jp

Masayuki Nakao
Department of Mechanical Engineering,
The University of Tokyo,
71D3, 2nd Bldg -Eng.,
7-3-1 Hongo, Bunkyo-ku,
Tokyo 113-8656, Japan
e-mail: nakao@hnl.t.u-tokyo.ac.jp

Impedance-Based Performance Analysis of Micropatterned Polymer Electrolyte Membrane Fuel Cells

Micropatterns applied to proton exchange membranes can improve the performance of polymer electrolyte fuel cells; however, the mechanism underlying this improvement is yet to be clarified. In this study, a patterned membrane electrode assembly (MEA) was compared with a flat one using electrochemical impedance spectroscopy and distribution of relaxation time analysis. The micropattern positively affects the oxygen reduction reaction by increasing the reaction area. However, simultaneously, the pattern negatively affects the gas diffusion because it lengthens the average oxygen transport path through the catalyst layer. In addition, the patterned MEA is more vulnerable to flooding, but performs better than the flat MEA in low-humidity conditions. Therefore, the composition, geometry, and operating conditions of the micropatterned MEA should be comprehensively optimized to achieve optimal performance. [DOI: 10.1115/1.4053388]

Keywords: electrochemical engineering, fuel cells

1 Introduction

The ability of fuel cells to convert chemical energy from hydrogen into electricity makes them a key technology for attaining a hydrogen-based society. In particular, polymer electrolyte membrane fuel cells (PEMFCs) are widely recognized as the most significant type of fuel cells because of their practical application in fuel cell vehicles [1,2], owing to their favorable operation at low temperatures. It is, therefore, essential to further improve the efficiency and performance of PEMFCs to advance this technology and its applications.

However, the high costs of using precious metal catalysts in PEMFCs remain a significant hindrance to the growth of their applications [3]. These high costs can be lowered by improving the device performance, as doubling the generated power density per specific electrode area would halve the cost of the entire membrane electrode assembly (MEA). Increasing the contact area has frequently been proposed to improve performance, especially for electrochemical devices such as batteries, solid-oxide fuel cells, and solar cells [4–7]. This approach has also been applied to PEMFCs. O'Hayre et al. [8] were the first to propose increasing the membrane surface area; they focused on Pt-spattered fuel cells and increased the roughness of the electrolyte membrane with SiC paper. Bae et al. [9] employed a controlled line pattern with dimensions of $5 \mu m$ and $110 nm$ width and showed that the power density of the microscale-patterned sample was 30% higher than that of the conventional flat sample. However, the nanoscale-patterned sample exhibited a lower power density. Thus, they concluded that the improved performance resulted from the increased interfacial area between the catalyst layer and membrane. Aizawa et al. [10,11] employed pillar-like structures with sizes of $3–10 \mu m$ and proposed that the performance improved because the protons were transported through the pillars before reacting far from the membrane-catalyst interface, resulting in an efficient oxygen reduction reaction (ORR). Jeon et al. [12] applied micropatterns with various shapes and sizes ranging from $2–26 \mu m$, and demonstrated a maximum power density improvement of 73%. This improvement resulted from the shorter transport pathways for the reactants, resulting in additional triple-phase boundaries. Seol et al. [13] deposited a catalyst layer onto a hole-patterned membrane fabricated via plasma etching. More recently, micropatterns on membranes for water transport have gained attention from scholars. Kim et al. [14] used a prismatic membrane and fabricated an MEA by thinning a catalyst layer to reflect the prism shape. This resulted in a triangular space between the gas diffusion and catalyst layer, which led to enhanced water transportation. Ahn et al. [15] furthered this approach using a prism pattern and sprayed catalyst layer. The patterned MEA was stretched vertically with respect to the pattern to form cracks at the bottom of the triangles. They observed the water transport behavior of the MEA via in situ environmental scanning electron microscopy and proved that the water droplets gathered and grew at the cracks, which acted as water reservoirs and passages.

As detailed earlier, micropatterned MEAs can be fabricated using numerous methods, and the development of these methods has significantly improved the performance of the MEAs. Moreover, several different mechanisms have been proposed to explain how these micropatterns improve the performance of the PEMFCs. Therefore, a detailed evaluation of the physical phenomena that affect the PEMFC performance is required.

Electrochemical impedance spectroscopy (EIS) is a powerful technique for the measurement and analysis of PEMFCs. Numerous studies have employed EIS for characterization and mass transport analysis [16–20]. Heinzmann et al. [21,22] applied an advanced analytical method for impedance data analysis—distribution of relaxation times (DRT)—to deconvolute the losses in a commercial MEA. The DRT analysis revealed five peaks, each of which was assigned to a physical phenomenon that contributed to the polarization resistance of the cell. The DRT approach enabled the deconvolution and subsequent quantification of

processes such as gas diffusion, ORR, and proton transport in the ionomer in the catalyst layer. The analysis revealed that the ORR is the rate-limiting step at low current densities. Conversely, at elevated current densities, the gas diffusion becomes the dominant loss mechanism.

In this study, the effect of the micropatterns on the performance of MEAs and the mechanisms underlying the observed performance improvements were investigated. In the available literature, there is a lack of studies that have analyzed the positive and negative effects of micropatterning. The tradeoff aspect of the surface patterning method for PEMFC can be explained as follows.

The Butler–Volmer equation for PEMFCs is expressed as follows [3]:

$$i = i_0 \left[\exp\left(\frac{\alpha n F}{RT} \eta \right) - \exp\left(-\frac{(1-\alpha)nF}{RT} \eta \right) \right] \quad (1)$$

where i, i_0, α, n, F, η, R, and T represent the current density, exchanged current density, transfer coefficient, number of electrons transferred due to the reaction, Faraday constant, activation overvoltage, universal gas constant, and temperature, respectively. Using the approximation $\exp(x) \cong 1 + x$, Eq. (1) can be transformed as follows:

$$i = \frac{nF i_0}{RT} \eta \quad (2)$$

Since the activation overvoltage can be expressed as $\eta = \Phi_P - \Phi_e - U_{ORR}$, it is a linear expression of the proton potential. For the utilization of catalyst particles, evaluating the percentage of particles attributed to the chemical reaction is important. This percentage of the particles is defined as the effectiveness factor. We would like to deploy this idea to PEMFC catalyst layer. The effectiveness factor of the first order reaction in the flat plane is represented as follows [23]:

$$E = \frac{\tanh \phi}{\phi} \quad (3)$$

$$\phi = L \sqrt{\frac{k}{D}} \quad (4)$$

where ϕ, L, k, and D represent the Thiele number, average diffusion length, reaction rate constant, and diffusion coefficient, respectively. In contrast, the oxygen concentration is included in effective i_0 as a linear function; therefore, its effectiveness factor is the same as that of the proton transport. Figure 1 shows a schematic of the
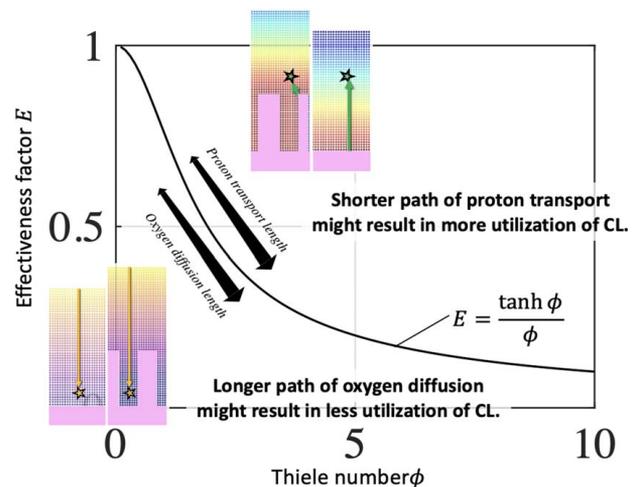
Fig. 1 Schematics of the surface patterning and effectiveness factor illustrating the expected positive and negative effects of patterning

	Gas supply (sccm)				Temperature (°C)		Humidification	
	Ca. O_2	Ca. N_2	Ano. H_2	Ano. N_2	Cell	Bubbler	RH (%)	Total flowrate (sccm)
Current density variation	40	110.6	120	30.6	70	65	80.2	200
pO_2 variation	60	90.6	120	30.6	70	65	80.2	200
	120	30.6	120	30.6	70	65	80.2	200
	20	130.6	120	30.6	70	65	80.2	200
RH variation	40	116.9	120	36.9	70	62	70.0	200
	40	122.4	120	42.4	70	59	61.0	200
	40	128.9	120	48.9	70	55	50.4	200
	40	134.4	120	54.4	70	51	41.5	200

surface patterning and effectiveness factor. The use of the surface patterning method reduces the proton transport length. Therefore, the value of L in Eq. (4) decreases, which results in an increase in the effectiveness factor. However, the oxygen transport length increases during surface patterning. Therefore, the effectiveness factor of oxygen decreases.

This study aims to understand the detailed mechanisms by which patterned MEAs improve the PEMFC performance and is expected to be the first step in their optimization. To achieve these objectives, EIS and DRT analyses were performed to compare patterned and flat MEAs. We focused on both the positive and negative effects of applying micropatterning to MEAs and on understanding the detailed mechanism of the observed performance improvements.

2 Experimental

2.1 Membrane Electrode Assembly Fabrication and Cell Assembly.
A cathode-micropatterned MEA was fabricated by preparing a line-patterned membrane using a thermal imprinting process. A micropatterned Ni mold (5 μm line pattern) was prepared, which was replicated to Nafion (NRE-212, Sigma-Aldrich Co. LLC) by hot pressing at 5 MPa and 110 °C. To treat the flat MEA similarly, a flat plate of Ni was prepared, and the same thermal imprinting process was employed. The catalyst ink was prepared by mixing Pt-loaded carbon (TEC10V50E, Tanaka Kikinzoku Kogyo K.K.), water, isopropyl alcohol, and an ionomer dispersion (DE1021 CS type, FUJIFILM Wako Pure Chemical Co.) (Table S1 available in the Supplemental Materials on the ASME Digital Collection). The ionomer-to-carbon weight ratio was 1.0. The ink was air-sprayed onto the thermally imprinted membrane at 70 °C. The completed MEA was dried on a hot plate at 70 °C for 5 min. The area of the catalyst layer was 10 × 10 mm, and the Pt loading was 0.4 mg cm^{-2}. The MEA was soaked in water for at least 10 h before cell assembly in a commercial cell housing (FC-02-01, ElectroChem Inc.) with a serpentine flow field. The fabricated MEA and commercial gas diffusion layer (Sigracet® 29BC, SGL carbon GmbH) were sandwiched between the housing using a polytetrafluoroethylene gasket to prevent gas leakage. The thicknesses of the gas diffusion layer and gaskets were 220 and 200 μm, respectively. Both MEA samples were removed from their housing after all measurements. Cross-sectional samples were acquired by cracking the samples after freezing in liquid nitrogen and observed via scanning electron microscopy (SEM, SU8010, Hitachi High-Technologies Co.).

2.2 Measurements.
Three types of measurements were conducted under different operating conditions (Fig. S1 available in the Supplemental Materials on the ASME Digital Collection). The operating temperature was adjusted using a ceramic heater attached to the housing. The gas flow line was equipped with two mass flow controllers for each cathode and anode gas line. The oxygen and nitrogen flowrates were controlled at the cathode gas line similar to the hydrogen and nitrogen flowrates at the anode gas line, between

0 and 200 sccm under the standard condition (0 °C). The gases were supplied to the MEA at 0.1 MPa. Both the cathode and anode gas lines were humidified using bubblers. The relative humidity (RH) was adjusted using the dew point difference between the operating and bubbler temperatures. Before performing the measurements, the cell was subjected to conditioning using repeated galvanodynamic polarization for approximately 24 h until the polarization curve showed no further increase in cell voltage.

After conditioning, a current density variation analysis was performed at current densities ranging from 0.02 to 1.00 A cm^{-2}. The total gas flowrate was maintained at 200 sccm for both the cathode and anode during all measurements. The RH was 80%, while the hydrogen and oxygen partial pressures were 0.6 and 0.2 atm, respectively. The operating conditions are detailed in Table 1. The cell was operated galvanostatically at the desired target current density for 30 min to perform EIS under stable conditions. The polarization curves were acquired using the measured cell voltage and current density data after 30 min of operation. EIS was performed galvanostatically with sweeping between 0.1 Hz and 1 MHz; subsequently, the current density was set to the next value.

The effect of varying the oxygen partial pressure (expressed as pO_2) from 0.1 to 0.6 atm was then analyzed. A current density of 0.84 A cm^{-2} was employed because it was assumed that pO_2 has a significant effect in the high-current region. The hydrogen partial pressure (expressed as pH_2) and RH were 0.6 atm and 80%, respectively. The stabilizing operation and EIS were performed in the same manner as the current density analysis described.

Finally, RH variation analysis was performed at 40–80% RH Low (0.05 A cm^{-2}) and high (0.84 A cm^{-2}) current densities were selected to perform galvanostatic EIS. The pH_2 and pO_2 were 0.6 and 0.2 atm, respectively. Under each target RH, the stabilizing operation and EIS were initially performed at the low current, and subsequently, at the high current. The target RH was then set to the next value after every set of these two measurements.

2.3 Kramers–Kronig and Distribution of Relaxation Time Analyses.
The Kramers–Kronig test [24,25] is frequently used to evaluate the validity of measured impedance spectra and determine whether the data include noise. Causality, linearity, and time-invariant conditions result in a complex dataset that obeys a real and imaginary relationship as follows:

$$Z_{Re}(\omega) = \frac{2}{\pi} \int_0^\infty \frac{\omega' \cdot Z_{Im}(\omega')}{\omega^2 - \omega'^2} d\omega' \quad (5)$$

$$Z_{Im}(\omega) = -\frac{2}{\pi} \int_0^\infty \frac{\omega \cdot Z_{Re}(\omega')}{\omega^2 - \omega'^2} d\omega \quad (6)$$

where $Z_{Re}(\omega)$ and $Z_{Im}(\omega)$ represent the real and imaginary parts of the impedance, respectively, and ω represents the angular frequency. These equations indicate that the imaginary part can be calculated using the real part and vice versa. The Kramers–Kronig test uses these calculated values to validate the data quality by

comparing the measured and calculated impedances and obtain residuals. We conducted a Kramers–Kronig test using Lin–KK tools [26] from the Karlsruhe Institute of Technology to validate the data quality. The data points with a frequency greater than 105 were removed from latter analyses as they showed high residuals, thereby indicating noise (Fig. S2 available in the Supplemental Materials on the ASME Digital Collection).

Fuoss and Kirkwood first proposed the concept of DRT analysis [27]. Schichlein et al. applied it to PEMFCs and performed the electrochemical characterization [28]. In this study, DRT analysis was conducted using the DRT tools created by Wan et al. [29]. The relationship between the complex impedance $Z(\omega)$ and distribution function of relaxation times $g(\tau)$ is expressed as follows:

$$Z(\omega) = R_0 + \int_0^\infty \frac{g(\tau)}{1 + j2\pi f\tau} d\tau \qquad (7)$$

where R_0 and R_{pol} represent the ohmic and polarization resistances, respectively, and $\tau = RC$ is the time constant of an RC element. In the DRT analysis, the impedance $g(\tau)$ is represented by a weighted series of RC elements. In the impedance measurement, data are commonly acquired on the logarithmic scale. Subsequently, Eq. (7) is rewritten as follows:

$$Z(\omega) = R_0 + \int_0^\infty \frac{\gamma(\ln \tau)}{1 + j2\pi f\tau} d\tau \qquad (8)$$

where $\gamma(\ln\tau) = \tau g(\tau)$. DRT tools are used to calculate the DRT function by minimizing the polarization resistance difference between the experimental data and estimated DRT, which is expressed as the sum of the radial basis functions. The detailed calculation methods have been explained in a previous study [29].

The resulting graph of function $\gamma(\tau)$ is beneficial for deconvoluting the chemical reaction and mass transport processes with close time constants. Further details about DRT and its application to porous electrodes can be found in previous publications [30–32]. Additionally, to determine the validity of the acquired DRT results, an algorithm based on Tikhonov regularization was implemented [33,34]. The obtained results were in excellent agreement with the DRT results.

There are three methods of analyzing and comparing the DRTs. The first is based on the quantification of the area under the peaks. Since the area under each peak corresponds to the polarization resistance of the related electrochemical process, it is the most direct method for a quantitative analysis. However, in the case of overlapping peaks, this approach is prone to errors. The second method involves the complex nonlinear least-square fitting of a physicochemically meaningful equivalent circuit model (ECM) to the measured spectra and then comparing the ECM elements. This method requires a physicochemically meaningful ECM and might include errors due to the fitting procedure. The third method involves a qualitative comparison of the peaks in the DRT graph. Heinzmann et al. used this method in their study [21]. As described earlier, the area below the peak corresponds to the related polarization resistance. If the peak shapes are similar, it is sufficient to compare the peak height instead of the area under the peak. In this study, the peak comparison method is discussed in Sec. 3.

3 Results and Discussion

3.1 Sample Observation and Polarization Curves.
Figures 2(a) and 2(b) show the cross-sectional SEM images of the patterned and flat MEA, respectively. The membrane was slightly deformed from the original shape of the Ni mold (5 μm line pattern) during the measurements because of the housing pressure or operating temperature. However, the micropattern remained present during the measurements; thus, the acquired results reflect the effect of the patterned membrane.

Figure 3 shows the measured polarization curves. In the low-current density region, where the ORR is dominant, the patterned membrane shows a higher cell voltage at the same current density level than the conventional flat sample. Conversely, in the high-current density region, where the gas diffusion is dominant, the flat sample outperformed the patterned sample, which underwent a steep drop in cell voltage. This result suggests that the physical phenomena, which are illustrated in Figs. 1(a) and 1(b), are plausible hypotheses.

3.2 Current Density Analysis.
Figures 4(a)–4(c) show the impedance spectra in the low-current and high-current density regions and the corresponding DRT results of the patterned MEA, respectively. The results for the flat MEA are shown in Figs. 4(d)–4(f). In this study, all the fitted lines of the impedance spectra were obtained as output from the DRT tools and are calculated based on discretized radial-based functions [29]. In the low-current-density region, the polarization resistance and DRT peaks of the patterned MEA are slightly smaller than those of the flat MEA at the very-low-current density region; otherwise, the impedance spectra and DRT peaks of the patterned and flat MEAs in the low-current-density region are largely identical (see also Fig. S3 available in the Supplemental Materials on the ASME Digital Collection). The authors recognize the importance to perform the experiment repeatedly in future works to ensure that the patterned sample is superior to the flat one. Conversely, in the high-current-density region, the results are significantly different. The polarization resistance decreased as the current density increased. However, when the current density exceeded 0.5–0.6 A cm^{-2}, the polarization resistance gradually increased. This tendency was observed in both the patterned and flat MEAs, but to significantly different degrees (black arrows in Figs. 4(b)–4(e), respectively). The cell voltage of both types of MEAs is nearly identical at 0.84 A/cm^2 but the slope of the polarization curves differs, while the polarization resistance difference is visible in impedance spectra. In the high-current region, a DRT peak around 10–100 Hz splits into two peaks, which is more pronounced in the flat MEA (Fig. 4(f)). According to a previous study on the DRT analysis [21], it can be assumed that this peak represents the contribution of the gas diffusion to the polarization resistance. Moreover, the lower frequency peak represents the contribution of the gas diffusion to the polarization resistance, and the higher frequency peak represents that of the ORR. The gas diffusion peak of the patterned MEA shows a more significant increase than that of the flat MEA (gray box in Figs. 4(c)–4(f)). These results indicate that the contribution of gas diffusion toward the polarization resistance in the patterned sample was more significant than that in the flat sample. This result supports the hypothesis from Fig. 1(b).
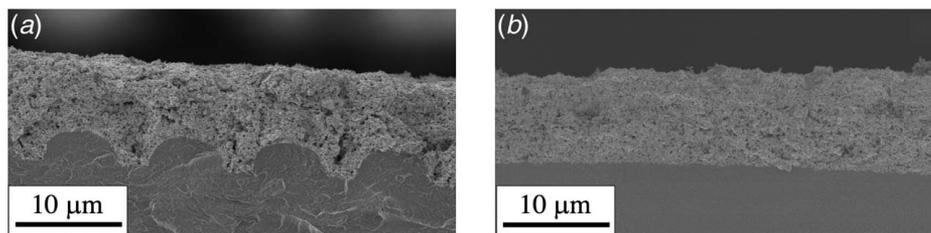
Fig. 2 Cross-sectional SEM images of the (a) patterned and (b) flat MEAs
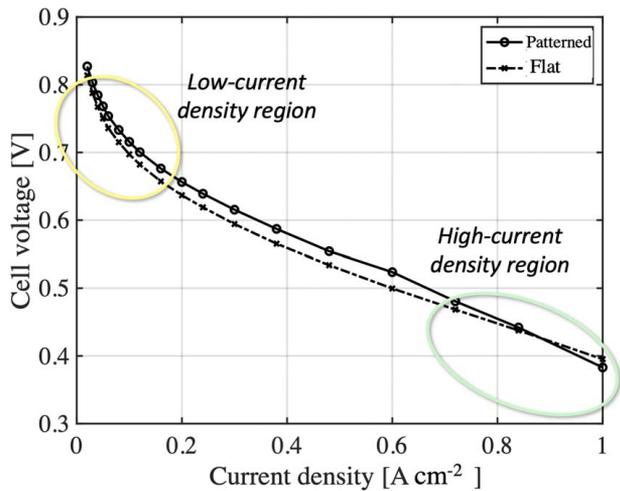
Fig. 3 Polarization curves of the patterned (solid line) and flat (dashed line) MEAs

3.3 Oxygen Partial Pressure Analysis.

In the oxygen partial pressure variation experiment, four impedance datasets were measured at different pO$_2$ ranging from 0.1 to 0.6 atm. However, the dataset acquired at 0.1 atm was excluded from subsequent discussions as it contained excessive noise, as shown in Fig. S4 available in the Supplemental Materials on the ASME Digital Collection. This is because the combination of a low pO$_2$ and high current density was extremely harsh for the stable operation of the MEA samples.

Figure 5(a) shows the impedance spectra of the patterned MEA under different pO$_2$ at an RH and current density of 80% and 0.84 A cm^{-2}, respectively; Fig. 5(b) shows the corresponding DRT results. The polarization resistance significantly decreased with increasing pO$_2$ because the ORR occurs readily under oxygen-

rich conditions [3]. Figures 5(c) and 5(d) show the impedance spectra of the flat MEA under the same conditions and the corresponding DRT results, respectively. The polarization resistance of the patterned MEA was larger than that of the flat MEA; however, the difference between them decreased as pO$_2$ increased (broken line connecting Figs. 5(a)–5(c)). The measurements were conducted in the high-current-density region, where gas diffusion is crucial; oxygen diffusion was the dominant rate-controlling process under such conditions, limited by a rich oxygen supply. In summary, the patterned MEA did not perform well at high current densities under oxygen-poor conditions, but performed as well as the flat MEA under oxygen-rich conditions.

The current density variation section (Fig. 4(f)) of the flat MEA shows two peaks between 10 and 10^3 Hz, assigned to the gas diffusion and ORR in ascending order (Fig. 5(d)). The gas diffusion peak significantly increased with decreasing pO$_2$. A marked difference in this peak was observed between the patterned and flat MEAs. The peak of the patterned MEA exhibited a more pronounced increase (arrow in Fig. 5(b)), indicating that the performance of the patterned MEA was more sensitive to changes in the oxygen levels. This result indicates that the micropattern on the membrane hindered oxygen transport.

In summary, the micropatterns slightly improved the PEMFC performance in the low- to middle-current density regions. However, they may interfere with gas diffusion, especially under conditions with high oxygen requirements, such as high-current operation and oxygen-poor conditions. This situation could be solved by ensuring a rich supply of oxygen. According to Akitomo et al. [35], pressurized gas is often supplied to the cathode electrode in fuel cell vehicles to alleviate the gas diffusion limitation. Therefore, micropatterned MEAs might be suitable for such applications.

3.4 Relative Humidity Analysis.

Figures 6(a) and 6(b) show the impedance spectra of the patterned MEA under different RH conditions in the low-current-density region (0.05 A cm^{-2}) and
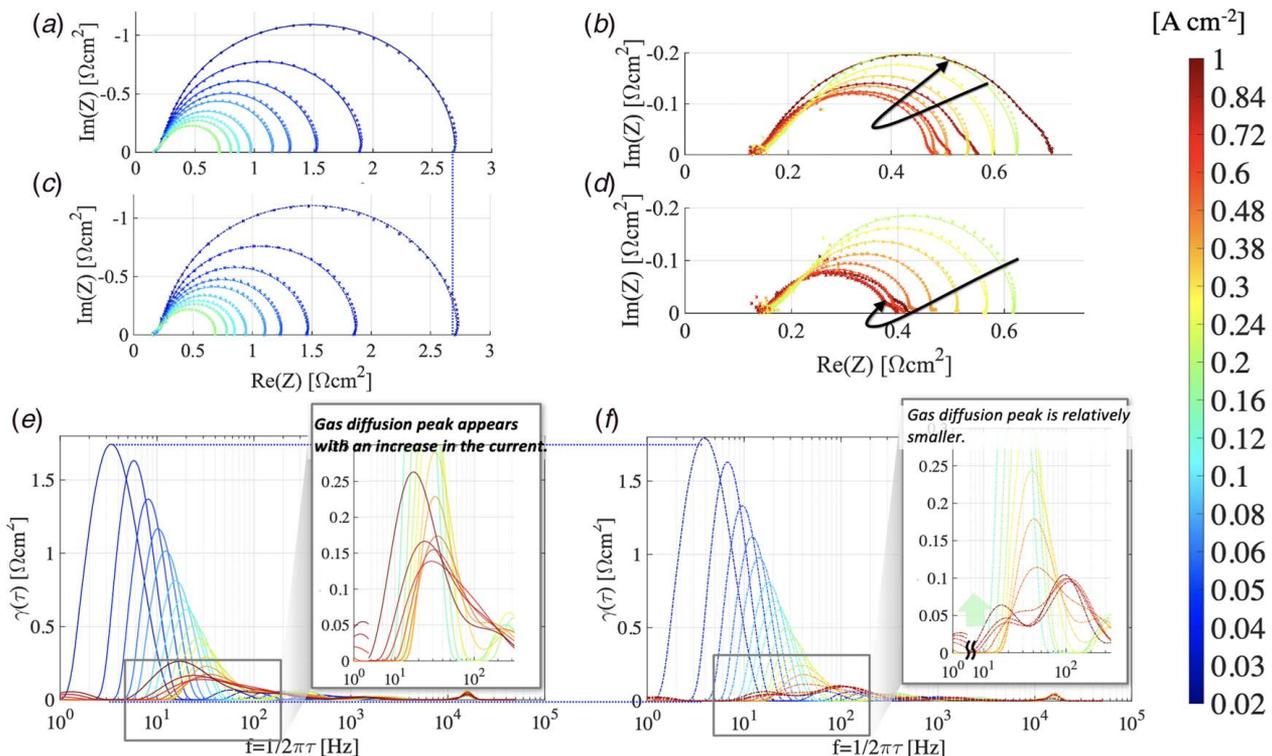
Fig. 4 Current density analysis from 0.02 to 1.00 A cm^{-2} at 80% RH and pO$_2$ = 0.2 atm. Impedance spectra (original datapoints with fitted lines) in the (a) and (d) low-current density region and (b) and (e) high-current density region. Corresponding DRT results for the (a)–(c) patterned and (d)–(f) flat MEAs
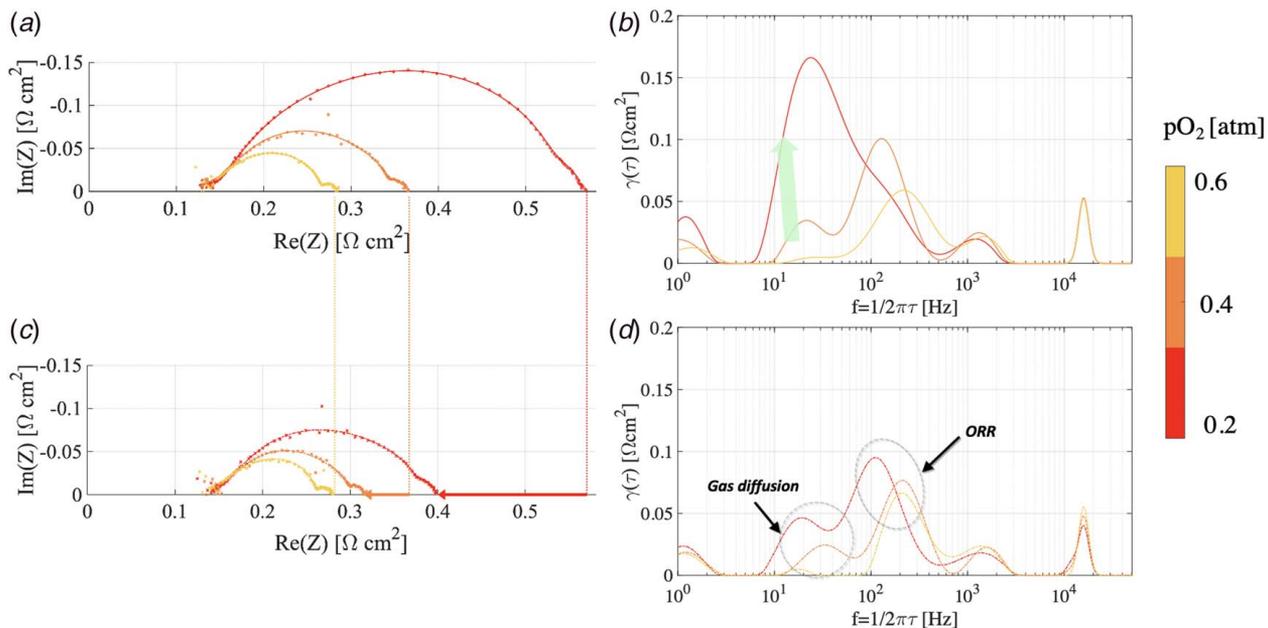
Fig. 5 Oxygen partial pressure analysis at 0.84 A cm^{-2} and 80% RH (*a*) and (*c*) Impedance spectra (original data points with fitted lines) and (*b*) and (*d*) corresponding DRT results for the (*a*) and (*b*) patterned and (*c*) and (*d*) flat MEAs
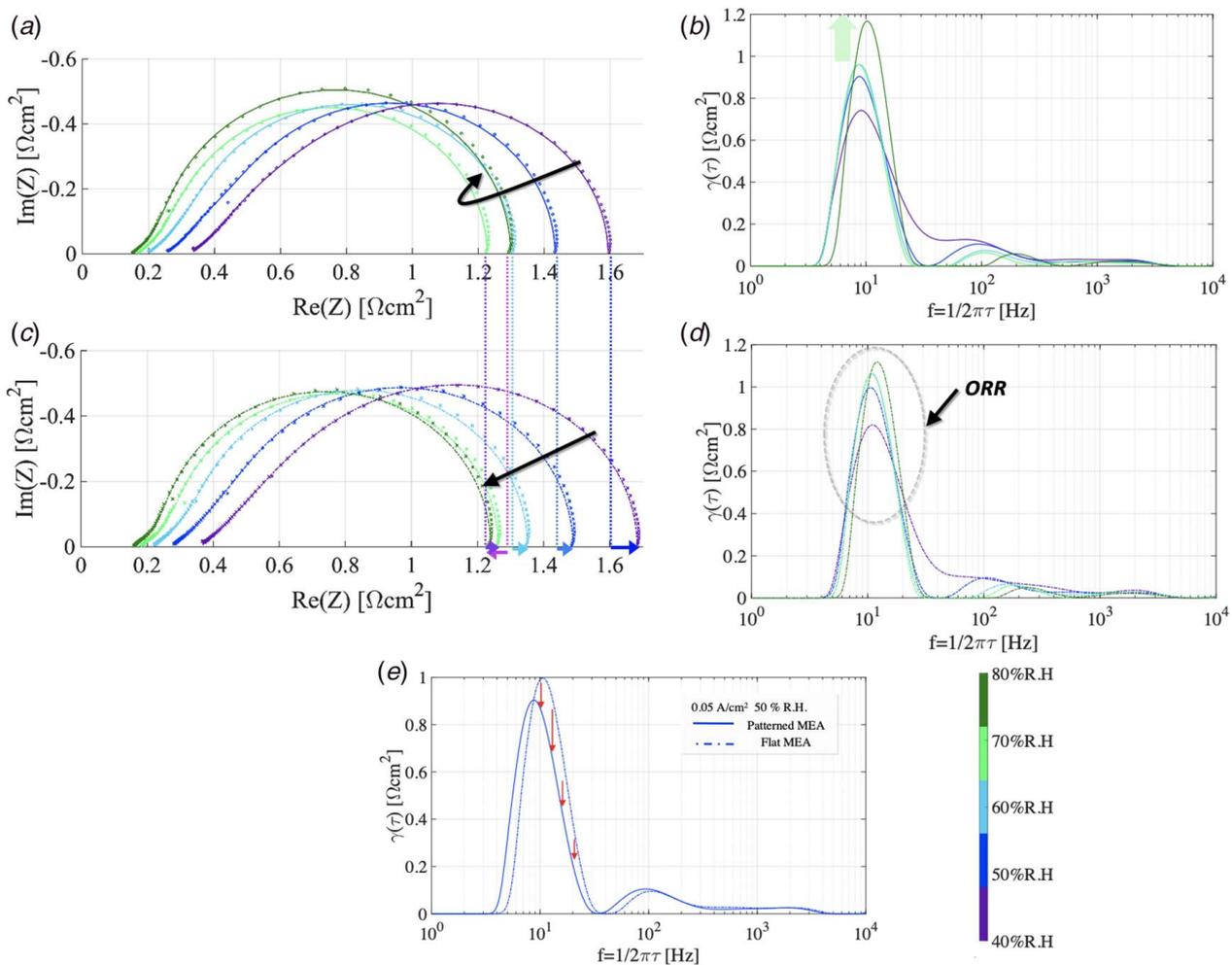
Fig. 6 Relative humidity analysis at 0.05 A cm^{-2}. (*a*) and (*c*) Impedance spectra (original data points with fitted lines) and (*b*) and (*d*) corresponding DRT results for the (*a*) and (*b*) patterned and (*c*) and (*d*) flat MEAs, and (*e*) DRT results comparison at 50% RH

the corresponding DRT results, respectively. Both the ohmic and polarization resistances decreased as the RH increased; however, the polarization resistance increased at 80% RH. It can be assumed that a higher humidity moistens the membrane and ionomer, facilitating proton transport. However, high-humidity conditions will easily flood the catalyst layer [36] and block the reaction area. Therefore, an increase in the polarization resistance implies that flooding is crucial at 80% RH. The DRT results also supported this hypothesis. The peak at approximately 10 Hz, which indicates the contribution of the ORR to the polarization resistance, was significantly larger at 80% RH (light-green arrow in Fig. 6(b)).

Figures 6(c) and 6(d) show the impedance spectra of the flat MEA and corresponding DRT results, respectively. In contrast to the results obtained for the patterned MEA, the polarization resistance of the flat MEA decreased linearly as the RH increased. Considering that the ohmic resistances of the patterned and flat MEAs were the same at each RH, the polarization resistance of the patterned MEA was smaller at 40–70% RH. Simultaneously, it was greater at higher RH (dashed lines connecting Figs. 6(a)–6(c)). This result suggests two inferences. The first inference is that micropatterns are especially effective at lower RH. An increase in the membrane surface area creates more paths for charge transport. It can be assumed that the proton transport paths were the most affected because the patterned MEA performed better than the flat MEA at low RH. The other inference is that the flat sample is more suitable for water-condensable conditions. The micropatterns are more susceptible to flooding because the catalyst-embedded powders will be inactive if the water blocks the pattern entries (Fig. S5 available in the Supplemental Materials on the ASME Digital Collection). Figure 6(e) compares the DRT results of the patterned and flat MEAs at 50% RH. The peaks at 10 Hz, which correspond to the ORR contribution toward the polarization resistance, indicate that the patterned MEA had a lower ORR resistance than the flat MEA. This suggests that the hypothesis shown in Fig. 1(a) is entirely plausible.

Figures 7(a) and 7(b) show the impedance spectra of the patterned MEA under different RH conditions in the high-current-density region (0.84 A cm^{-2}) and the corresponding DRT results, respectively. Changing the humidity had the same effect on the impedance spectra as it did in the low-current-density region, where the polarization resistance decreased between 40 and 70% RH, and then increased at 80% RH. The ohmic resistance showed a monotonic decrease with increasing RH. Figures 7(c) and 7(d) show the impedance spectra of the flat MEA under the same conditions and the corresponding DRT results, respectively. Furthermore, in contrast to the observation in the low-current-density region, the polarization resistance of the flat MEA increased at 80% RH. More water would be present under high-current-density operations because more chemical reactions are required. Therefore, even the flat MEA suffered from flooding. The most significant difference between the DRT results of the patterned and flat MEAs was the peak at approximately 20 Hz, which is speculated to be the contribution of gas diffusion to the polarization resistance. This suggests that oxygen transport in the patterned MEA is hindered to a greater degree, thereby supporting the hypotheses in Fig. 1(b).

Moreover, in Figs. 5(b)–5(d) and 7(b)–7(d), a peak was observed at 10^0 Hz in the impedance spectra of the patterned MEA. The origin of this peak is still unclear; however, it can be assumed that the water transport phenomena may be responsible for its occurrence because the peak height exhibits a dependency on RH but not on the pO$_2$. According to Pivac and Barbir [37], there are some previous studies that associate the inductive phenomena in the impedance spectra at low frequencies with water-transport-related phenomena, which cause low frequency impedances. Wiezell et al. reported that water profiles within the electrolyte membranes mainly cause low frequency inductive loops [38]. In contrast, Schneider et al. reported that the impedance is associated with the slow uptake and release of water into and from the electrolytes or ionomers [39]. Holmström et al. claimed that the occurrence of the inductive loops can be attributed to the dehydration and rehydration of the anode [40]. In short, the origin of the low frequency peak at approximately 10^0 Hz remains undetermined. However, our results indicate that this peak occurred due to water-transport-related phenomena.

The humidity variation test suggested that the patterned MEA functions better under lower-humidity conditions; in other words, better proton transport is advantageous. (Here, please note that better proton transport results in the improved charge transfer kinetics of ORRs. The proton transport resistance itself invokes higher frequency peaks, such as those at 10^3 Hz.) Ionomer loading in the catalyst layer is a critical feature in improving the performance of the PEMFCs. Certain studies investigating the effect of ionomer content and its optimization [41–44] have shown that increasing the ionomer content facilitates proton transport. However, simultaneously, more ionomers result in fewer oxygen transport paths
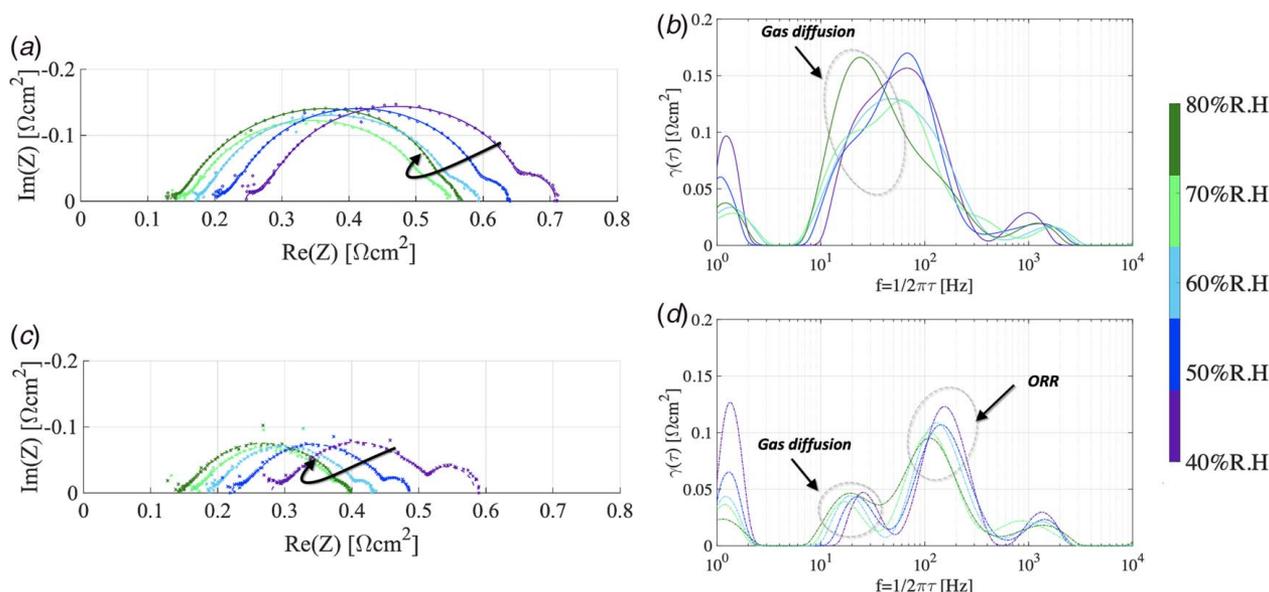
Fig. 7 Relative humidity analysis at 0.84 A cm^{-2}. (a) and (c) Impedance spectra (original data points with fitted lines) and (b) and (d) corresponding DRT results for the (a) and (b) patterned and (c) and (d) flat MEAs

because they replace the pores in the catalyst layer. Therefore, it is essential to compromise for this tradeoff. Low-humidity conditions severely affect proton transport, and thus, require a relatively high ionomer content.

In summary, our results suggest that patterned MEAs are suitable for fuel cell applications, as they typically do not involve a humidifier, especially for mobile usage [45]. Furthermore, low-humidity conditions are typical in fuel cell applications. We also observed that patterned MEAs might require a lower ionomer content to ensure appropriate gas diffusion than conventional flat MEAs.

In this study, we investigated various aspects of patterned MEAs and observed that they are susceptible to gas diffusion and water flooding. However, we also noted that patterned MEAs exhibit better proton transport owing to an increase in the surface area, which indicates that the ionomer content can be reduced to achieve better gas diffusion and prevent flooding. The comprehensive optimization of factors, including the micropattern geometry, catalyst composition, and operating conditions, would be necessary to fully utilize the surface-patterning method.

4 Conclusions

Patterned and flat MEAs were fabricated using a thermal imprinting process using flat Ni plate pressing. A 5 μm line pattern was used for micropatterning. The SEM images obtained after the entire measurement procedure confirmed that the micropatterns were preserved during the measurements. Furthermore, EIS and DRT analyses were performed to compare the patterned and flat MEAs.

The polarization curves showed that the patterned MEA performed better than the conventional flat MEA. The current density analysis indicated that the patterned MEA experienced hindered gas diffusion; the pO$_2$ analysis further supported this deduction. Conversely, the humidity analysis showed that the patterned MEA functions better than the flat MEA, especially under low-humidity operating conditions. The corresponding DRT results revealed that the ORR was improved by micropatterning.

The key findings of this study are presented as follows:

– Patterning the MEA had both positive and negative effects. The former is related to the improved ORR owing to the increased proton transport paths, whereas the latter is related to the vulnerability toward gas diffusion and flooding.
– The patterned MEA should be operated under favorable conditions to maximize the advantages of patterning. The patterned MEA is suitable for mobile fuel cell applications owing to its high performance under low-humidity conditions.
– The positive and negative aspects of the MEA's mechanism of action support the assumption that the patterned MEA would require an optimized catalyst layer composition. The ionomer content can be reduced to overcome the drawbacks of gas diffusion and flooding because the micropattern ensures sufficient proton transport paths.

Our future work will focus on two avenues of research. First, we will conduct a numerical analysis of the electrochemical properties to explore the mechanisms for improving the performance of MEAs using the surface patterning method. Visualization of the mass transport, electrochemical reactions, and current density demands investigation, as the findings of this study suggest that an increase in the surface area contributes to improved proton transport. The other proposed approach would focus on investigating the optimal composition and most suitable operating conditions for patterned MEAs. Our study suggests that the ideal ionomer content of patterned MEAs may differ from that of conventional flat MEAs.

Furthermore, optimizing the operating conditions is vital for achieving high power density, as we observed that the patterned MEA worked well under specific conditions. Every relevant previous study has reported a significant improvement in power density

upon using the surface patterning method; however, the improvement was in the range of approximately 10–70%. Therefore, comprehensive optimization of the composition and operating conditions should enable stable improvement or higher power densities.

Conflict of Interest

There are no conflicts of interest.

Nomenclature

i = current density
k = reaction rate constant
n = number of electrons transferred due to the reaction
D = diffusion coefficient
E = effectiveness factor
F = Faraday constant
L = average diffusion length
R = universal gas constant
T = temperature
i_0 = exchange current density
R_0 = Ohmic resistances
R_{pol} = polarization resistances
$Z_{Re}(\omega)$ = real parts of the impedance
$Z_{Im}(\omega)$ = imaginary parts of the impedance
α = transfer coefficient
η = activation overvoltage
φ = thiele number
ω = angular frequency
∞ = infinity

References

[1] Mehta, V., and Cooper, J. S., 2003, "Review and Analysis of PEM Fuel Cell Design and Manufacturing," J. Power Sources, 114(1), pp. 32–53.
[2] Sharaf, O. Z., and Orhan, M. F., 2014, "An Overview of Fuel Cell Technology: Fundamentals and Applications," Renew. Sustain. Energy Rev., 32, pp. 810–853.
[3] O'Hayre, R., Cha, S., Colella, W., and Prinz, F. B., 2009, Fuel Cell Fundamentals, John Wiley & Sons Inc, New York.
[4] He, Y., Yu, X., Wang, Y., Li, H., and Huang, X., 2011, "Alumina-Coated Patterned Amorphous Silicon as the Anode for a Lithium-Ion Battery With High Coulombic Efficiency," Adv. Mater., 23(42), pp. 4938–4941.
[5] Kim, J., Koh, J. K., Kim, B., Kim, J. H., and Kim, E., 2012, "Nanopatterning of Mesoporous Inorganic Oxide Films for Efficient Light Harvesting of Dye-Sensitized Solar Cells," Angew. Chemie—Int. Ed., 51(28), pp. 6864–6869.
[6] Herbstritt, D., Weber, A., and Ivers-Tiffée, E., 2001, "Modelling and DC-Polarisation of a Three Dimensional Electrode/Electrolyte Interface," J. Eur. Ceram. Soc., 21(10–11), pp. 1813–1816.
[7] Nagato, K., Shinagawa, S., Shikazono, N., Iwasaki, S., and Nakao, M., 2015, "SOFC Anode Based on YSZ Pillars," ECS Trans., 68(1), pp. 1309–1314.
[8] O'hayre, R., Lee, S. J., Cha, S. W., and Prinz, F. B., 2002, "A Sharp Peak in the Performance of Sputtered Platinum Fuel Cells at Ultra-low Platinum Loading," J. Power Sources, 109(2), pp. 483–493.
[9] Bae, J. W., Cho, Y. H., Sung, Y. E., Shin, K., and Jho, J. Y., 2012, "Performance Enhancement of Polymer Electrolyte Membrane Fuel Cell by Employing Line-Patterned Nafion Membrane," J. Ind. Eng. Chem., 18(3), pp. 876–879.
[10] Aizawa, M., Gyoten, H., Salah, A., and Liu, X., 2010, "Pillar Structured Membranes for Suppressing Cathodic Concentration Overvoltage in PEMFCs

at Elevated Temperature/low Relative Humidity," J. Electrochem. Soc., **157**(12), p. B1844.

[11] Aizawa, M., and Gyoten, H., 2013, "Effect of Micro-Patterned Membranes on the Cathode Performances for PEM Fuel Cells Under low Humidity," J. Electrochem. Soc., **160**(4), pp. F417–F428.

[12] Jeon, Y., Kim, D. J., Koh, J. K., Ji, Y., Kim, J. H., and Shul, Y. G., 2015, "Interface-Designed Membranes with Shape-Controlled Patterns for High-Performance Polymer Electrolyte Membrane Fuel Cells," Sci. Rep., **5**(1), pp. 1–11.

[13] Seol, C., Jang, S., Lee, J., Nam, L. V., Pham, T. A., Koo, S., Kim, K., Jang, J. H., Kim, M., and Yoo, S. J., 2021, "High-Performance Fuel Cells with a Plasma-Etched Polymer Electrolyte Membrane with Microhole Arrays," ACS Sustain. Chem. Eng., **9**(17), pp. 5884–5894.

[14] Kim, S. M., Kang, Y. S., Ahn, C., Jang, S., Kim, M., Sung, Y. E., Yoo, S. J., and Choi, M., 2016, "Prism-Patterned Nafion Membrane for Enhanced Water Transport in Polymer Electrolyte Membrane Fuel Cell," J. Power Sources, **317**(15), pp. 19–24.

[15] Ahn, C. Y., Jang, S., Cho, Y. H., Choi, J., Kim, S., Kim, S. M., Sung, Y. E., and Choi, M., 2018, "Guided Cracking of Electrodes by Stretching Prism-Patterned Membrane Electrode Assemblies for High-Performance Fuel Cells," Sci. Rep., **8**(1), pp. 1–9.

[16] Springer, T. E., Zawodzinski, T. A., Wilson, M. S., and Gottesfeld, S., 1996, "Characterization of Polymer Electrolyte Fuel Cells Using AC Impedance Spectroscopy," J. Electrochem. Soc., **143**(2), pp. 587–599.

[17] Jaouen, F., Lindbergh, G., and Wiezell, K., 2003, "Transient Techniques for Investigating Mass-Transport Limitations in gas Diffusion Electrodes: II. Experimental Characterization of the PEFC Cathode," J. Electrochem. Soc., **150**(12), p. A1711.

[18] Makharia, R., Mathias, M. F., and Baker, D. R., 2005, "Measurement of Catalyst Layer Electrolyte Resistance in PEFCs Using Electrochemical Impedance Spectroscopy," J. Electrochem. Soc., **152**(5), p. A970.

[19] Wagner, N., and Friedrich, K. A., 2009, "Application of Electrochemical Impedance Spectroscopy for Fuel Cell Characterization: PEFC and Oxygen Reduction Reaction in Alkaline Solution," Fuel Cells, **9**(3), pp. 237–246.

[20] Malevich, D., Halliop, E., Peppley, B. A., Pharoah, J. G., and Karan, K., 2009, "Investigation of Charge-Transfer and Mass-Transport Resistances in PEMFCs with Microporous Layer Using Electrochemical Impedance Spectroscopy," J. Electrochem. Soc., **156**(2), p. B216.

[21] Heinzmann, M., Weber, A., and Ivers-Tiffée, E., 2018, "Advanced Impedance Study of Polymer Electrolyte Membrane Single Cells by Means of Distribution of Relaxation Times," J. Power Sources, **402**(31), pp. 24–33.

[22] Heinzmann, M., Weber, A., and Ivers-Tiffée, E., 2019, "Impedance Modelling of Porous Electrode Structures in Polymer Electrolyte Membrane Fuel Cells," J. Power Sources, **444**(31), p. 227279.

[23] Thiele, E. W., 1939, "Relation Between Catalytic Activity and Size of Particle," Ind. Eng. Chem., **31**(7), pp. 916–920.

[24] Boukamp, B. A., 1995, "A Linear Kronig-Kramers Transform Test for Immittance Data Validation," J. Electrochem. Soc., **142**(6), pp. 1885–1894.

[25] Schönleber, M., Klotz, D., and Ivers-Tiffée, E., 2014, "A Method for Improving the Robustness of Linear Kramers-Kronig Validity Tests," Electrochim. Acta, **131**(10), pp. 20–27.

[26] Schönleber, M. https://www.iam.kit.edu/wet/english/Lin-KK.php

[27] Fuoss, R. M., and Kirkwood, J. G., 1941, "Electrical Properties of Solids. VIII. Dipole Moments in Polyvinyl Chloride-Diphenyl Systems," J. Am. Chem. Soc., **63**(2), pp. 385–394.

[28] Schichlein, H., Müller, A. C., Voigts, M., Krügel, A., and Ivers-Tiffée, E., 2002, "Deconvolution of Electrochemical Impedance Spectra for the Identification of Electrode Reaction Mechanisms in Solid Oxide Fuel Cells," J. Appl. Electrochem., **32**(8), pp. 875–882.

[29] Wan, T. H., Saccoccio, M., Chen, C., and Ciucci, F., 2015, "Influence of the Discretization Methods on the Distribution of Relaxation Times Deconvolution: Implementing Radial Basis Functions with DRT Tools," Electrochim. Acta, **184**(1), pp. 483–499.

[30] Dierickx, S., Weber, A., and Ivers-Tiffée, E., 2020, "How the Distribution of Relaxation Times Enhances Complex Equivalent Circuit Models for Fuel Cells," Electrochim. Acta, **355**(20), p. 136764.

[31] Jürgen, W., 1992, "A Reliable and Fast Method for the Solution of Fredhol Integral Equations of the First Kind Based on Tikhonov Regularization," Comput. Phys. Commun., **69**(1), pp. 99–111.

[32] Sonn, V., Leonide, A., and Ivers-Tiffée, E., 2008, "Combined Deconvolution and CNLS Fitting Approach Applied on the Impedance Response of Technical Ni/8YSZ Cermet Electrodes," J. Electrochem. Soc., **155**(7), p. B675.

[33] Weber, A., 2021, "Impedance Analysis of Porous Electrode Structures in Batteries and Fuel Cells," TM. Tech. Mess., **88**(1), pp. 1–16.

[34] Ivers-Tiffée, E., and Weber, A., 2017, "Evaluation of Electrochemical Impedance Spectra by the Distribution of Relaxation Times," J. Ceram. Soc. Jpn., **125**(4), pp. 193–201.

[35] Akitomo, F., Sasabe, T., Yoshida, T., Naito, H., Kawamura, K., and Hirai, S., 2019, "Investigation of Effects of High Temperature and Pressure on a Polymer Electrolyte Fuel Cell with Polarization Analysis and X-ray Imaging of Liquid Water," J. Power Sources, **431**(15), pp. 205–209.

[36] Nara, H., Momma, T., and Osaka, T., 2013, "Impedance Analysis of the Effect of Flooding in the Cathode Catalyst Layer of the Polymer Electrolyte Fuel Cell," Electrochim. Acta, **113**(15), pp. 720–729.

[37] Pivac, I., and Barbir, F., 2016, "Inductive Phenomena at low Frequencies in Impedance Spectra of Proton Exchange Membrane Fuel Cells—A Review," J. Power Sources, **326**(15), pp. 112–119.

[38] Wiezell, K., Gode, P., and Lindbergh, G., 2006, "Steady-State and EIS Investigations of Hydrogen Electrodes and Membranes in Polymer Electrolyte Fuel Cells," J. Electrochem. Soc., **153**(4), p. A749.

[39] Schneider, I. A., Bayer, M. H., Wokaun, A., and Scherer, G. G., "Impedance Response of the Proton Exchange Membrane in Polymer Electrolyte Fuel Cells," J. Electrochem. Soc., **155**(8), p. B783.

[40] Holmström, N., Wiezell, K., and Lindbergh, G., 2012, "Studying Low-Humidity Effects in PEFCs Using EIS," J. Electrochem. Soc., **159**(8), pp. F369–F378.

[41] Antolini, E., Giorgi, L., Pozio, A., and Passalacqua, E., 1999, "Influence of Nafion Loading in the Catalyst Layer of gas-Diffusion Electrodes for PEFC," J. Power Sources, **77**(2), pp. 136–142.

[42] Passalacqua, E., Lufrano, F., Squadrito, G., Patti, A., and Giorgi, L., 2001, "Nafion Content in the Catalyst Layer of Polymer Electrolyte Fuel Cells: Effects on Structure and Performance," Electrochim. Acta, **46**(6), pp. 799–805.

[43] Xie, J., Xu, F., Wood, D. L., and More, K. L., 2010, "Influence of Ionomer Content on the Structure and Performance of PEFC Membrane Electrode Assemblies," Electrochim. Acta, **55**(24), pp. 7404–7412.

[44] Andersen, S. M., and Grahl-Madsen, L., 2016, "Interface Contribution to the Electrode Performance of Proton Exchange Membrane Fuel Cells—Impact of the Ionomer," Int. J. Hydrogen Energy, **41**(3), pp. 1892–1901.

[45] Yoshida, T., and Kojima, K., 2015, "Toyota MIRAI Fuel Cell Vehicle and Progress Toward a Future Hydrogen Society," Electrochem. Soc. Interface, **24**(2), pp. 45–49.